Composition-tuned Pt-skinned PtNi bimetallic clusters as highly efficient methanol dehydrogenation catalysts

Ting-Wei Liao[1,*,‡,†], Anupam Yadav[1,‡], Piero Ferrari[1], Yubiao Niu[2], Xian-Kui Wei[3], Jerome Vernieres[2], Kuo-Juei Hu[1], Marc Heggen[3], Rafal E. Dunin-Borkowski[3], Richard E. Palmer[2], Kari Laasonen[4], Didier Grandjean[1,*], Ewald Janssens[1], and Peter Lievens[1,*]

[1] *Quantum Solid State Physics, Department of Physics and Astronomy, KU Leuven, Celestijnenlaan 200D, box 2414, BE-3001 Leuven, Belgium.*

[2] *College of Engineering, Swansea University, Bay Campus, Fabian Way, Swansea SA1 8EN, United Kingdom*

[3] *Ernst Ruska-Centre for Microscopy and Spectroscopy with Electrons and Peter Grünberg Institute Forschungszentrum Jülich GmbH, Jülich 52428, Germany*

[4] *Department of Chemistry and Materials Science, Aalto University, P.O. Box 16100, FI-00076 Aalto, Finland.*

ABSTRACT: Platinum is the most active anode and cathode catalyst in next-generation fuel cells using methanol as liquid source of hydrogen. Its catalytic activity can be significantly improved by alloying with 3d metals, although a precise tuning of its surface architecture is still required. Herein, we report the design of a highly active low temperature (below 0°C) methanol dehydrogenation anode catalyst with reduced CO poisoning, based on ultra-low amount of precisely-defined Pt_xNi_{1-x} (x = 0 to 1) bimetallic clusters (BCs) deposited on inert flat oxides by Cluster Beam Deposition (CBD). These BCs feature clear composition-dependent atomic arrangements and electronic structures stemming from their nucleation mechanism that are responsible for a volcano-type activity trend peaking at the $Pt_{0.7}Ni_{0.3}$ composition. Our calculations reveal that at this composition a cluster skin of Pt atoms with d-band centres downshifted by subsurface Ni atoms weakens the CO interaction that in turn triggers a significant increase in the methanol dehydrogenation activity.

INTRODUCTION

Low temperature proton exchange membrane fuel cells (PEMFC) and high temperature solid oxide fuel cells (SOFC) are emerging as efficient, low cost and environment-friendly solutions to harvest energy from diverse renewable sources, such as hydrogen, hydrocarbons, water, bio-fatty acids and bio-alcohols. Among these sources methanol is a promising energy raw material that can be either directly electro-oxidized to power direct methanol fuel cells (DMFCs) or easily thermo-catalytically decomposed or reformed in situ into a mixture of hydrogen and carbon monoxide that is then fed into a H_2 fuel cell. Methanol-based fuel cells (MFCs) are more reliable than conventional H_2 fuel cells, as liquid methanol is easier to store and transport than hydrogen gas.[1, 2] Although platinum is widely used as (electro)catalyst in the dehydrogenation of methanol (CH_3OH),[3, 4] its performance is limited by its modest stability and selectivity.[5-7] The three main drawbacks of platinum-based anode catalysts are their high cost as methanol bonds breaking requires large amounts of catalyst,[8] their low selectivity to generate hydrogen as end product, and their low stability in presence of carbon monoxide, a by-product of methanol dissociation (i.e. the CO poisoning effect).[9, 10] These crucial challenges require remediation in order to design future high performance fuel cell catalysts, for which fundamental understanding of the reaction kinetics at the atomic and molecular level are required. For this purpose, the reaction kinetics of model catalyst systems such as single Pt atoms,[11] Pt single crystals,[12-14] oxide-supported Pt thin films,[15] and Pt nanoparticles,[6, 7] have been investigated intensively.

Pt-alloy nanoparticles as fuel cell catalyst have shown higher activity and enhanced tolerance to CO poisoning. Several alloying materials such as Sn, Ru, Mo, Nb, W, Ag, and Ni have been investigated.[16-19] Despite these efforts, the underlying mechanism for the alloy-induced activity and tolerance to the CO poisoning effect is still under debate. Some studies suggest that the co-adsorption of CO and OH groups is responsible for the induced tolerance,[9] while others attribute the reduced CO poisoning mainly to alloying-induced alteration of the electronic structure of platinum.[20-22] Density functional theory calculations (DFT)[13, 23-25] and experiments on few-atom clusters in the gas phase[26, 27] support the latter interpretation. This controversy is largely due to the lack of clear understanding of the effect of alloying on the catalyst activity. Depending on the particle size, shape, composition, spatial atomic arrangement and method of preparation, the activity can change drastically emphasizing the need for using well-characterized

materials to identify the fundamental mechanisms at work. Pt-Ni bimetallic extended surfaces[28-31], nanostructures[32], nanoclusters and nanoparticles[8, 33, 34] that have shown enhanced activity for the oxygen reduction reaction (ORR) as methanol-tolerant cathode catalyst in fuel cell applications are also considered as promising anode-related (electro)catalysts. In most cases the investigated Pt-Ni nanomaterials are produced with (electro) chemical methods that often have a limited control over the systems size and composition. Furthermore, the involvement of stabilizing chemicals in wet chemistry, such as ligand molecules, greatly alters the intrinsic properties of nanomaterials, making the understanding of their composition- and structure-dependent activity more complex.[35-40]

Depositing preformed Pt-based bimetallic clusters/nanoparticles, with precisely-defined size, composition and surface coverages[41-44] on various oxide supports, using the Cluster Beam Deposition (CBD) technology could be one of the key solutions to design better fuel-cell catalysts.[45] Clusters are particles typically composed of less than a thousand atoms and have dimensions smaller than a few nanometres. They have unique magnetic,[46] optical,[47] and catalytic[44, 48-50] properties, distinct from those of the bulk phase, which make them promising candidates for numerous applications. Their catalytic properties can be enhanced by a synergistic combination of different elements such as earth abundant Ni and precious Pt metal, which can at the same time improve significantly their activity, reduce the CO poisoning effect and the usage of abundance-critical platinum.

In this study, we use a laser ablation CBD source[51, 52] to produce and deposit Pt_xNi_{1-x} bimetallic clusters (BCs) with an accurate control over their size and chemical composition. The BCs are deposited on two different supports, carbon TEM grids and native SiO_2 surfaces, with different coverages ranging from 5 % to 25 % cluster-projected area coverage (1 to 5 atomic monolayers, ML). Using a combination of high angle annular dark field scanning transmission electron microscopy (HAADF-STEM), X-ray photoelectron spectroscopy (XPS) and temperature programmed desorption (TPD), the cluster composition-dependent atomic arrangement, activity and CO poisoning in the methanol decomposition reaction are demonstrated. DFT calculations on selected sizes of the most promising $Pt_{0.7}Ni_{0.3}$ composition ($Pt_{353}Ni_{106}$ and $Pt_{417}Ni_{144}$) reveals that the increased catalytic activity and reduced CO poisoning effect by alloying Pt with Ni can be attributed to local d-band modifications of surface Pt-skin atoms by the presence of subsurface Ni atoms.

COMPOSITION-TUNED SEGREGATED STRUCTURE IN PT_XNI_{1-X} CLUSTERS

The size distribution of Pt_xNi_{1-x} BCs with x = 0.9, 0.7, 0.5, 0.3 and 0.1 was characterized by STEM. The distribution of the BCs average diameters in a sample of more than 300 clusters was measured for each Pt_xNi_{1-x} composition. A comparable size distribution (FWHMs of 1.4 nm) with an average diameter around 2.0 nm was found for all the compositions (Figure S1). In order to characterize the atomic arrangement in Pt_xNi_{1-x} BCs, STEM images with high resolution were collected for all compositions. Given the large atomic number difference between Pt (78) and Ni (28), the atomic arrangement of these two elements within the BCs can be revealed with good contrast by their HAADF intensity profile.[43, 53] If phase segregation occurs, the brighter and darker parts of the BCs can be assigned to Pt-rich and Ni-rich areas, respectively. **Error! Reference source not found.** presents selected STEM images of Pt_xNi_{1-x} BCs along with their normalised quantitative radial intensity profile integrated over the polar coordinates. Detailed inspection of the STEM images indicates that, except for the $Pt_{0.5}Ni_{0.5}$ composition that is mostly alloyed, a composition-dependent phase segregation is prominent in all BCs, where the minority and majority element prefers to concentrate in the core and shell of the BCs, respectively.

This composition-tuned phase segregated atomic arrangement found in Pt-Ni BCs suggests that their formation mechanism is governed by the preferential formation of binary few-atom clusters in the nucleation stage already proposed for Au_xAg_{1-x} BCs produced with the same source.[43] This is confirmed by computing and comparing the mixing energies defined as the binding energies of the small 4-atom Pt_3Ni_1, Pt_2Ni_2 and Pt_1Ni_3 BCs and their monometallic counterparts Pt_4 and Ni_4, present in the gas-phase at the initial stages of the BCs nucleation and growth. As in the Au-Ag system, DFT calculations show that the formation of binary 4-atom clusters is energetically more favourable than that of the monometallic ones (Figure S2). This strongly suggests that these stable binary few-atom Pt-Ni clusters will form and agglomerate before the monometallic ones, to form the BCs core enriched in the minority element. The remaining pure Pt or Ni few-atom clusters of the majority elements will then condense on the Pt-Ni nuclei to form the BC shell following the same composition-tuned segregation mechanism of a general character discussed earlier.[43] A

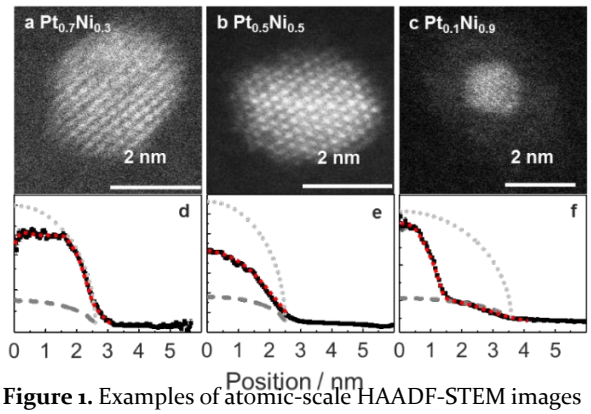

Figure 1. Examples of atomic-scale HAADF-STEM images of Pt_xNi_{1-x} BCs: (a, d) $Pt_{0.7}Ni_{0.3}$; (b, e) $Pt_{0.5}Ni_{0.5}$; (c, f) $Pt_{0.1}Ni_{0.9}$. The HAADF-STEM radial intensity profiles (d, e, f) are taken from the centre to the edge of the cluster and integrated from 0° to 360°. The red dotted lines correspond to simulations of cluster STEM intensity profiles with gradient composition evolution. The light grey dotted lines and dark grey dashed lines are simulated STEM intensities for pure Pt clusters and pure Ni clusters, respectively.

detailed comparison of the preparation and structure of Au-Ag and Pt-Ni systems is presented in Figure S3.

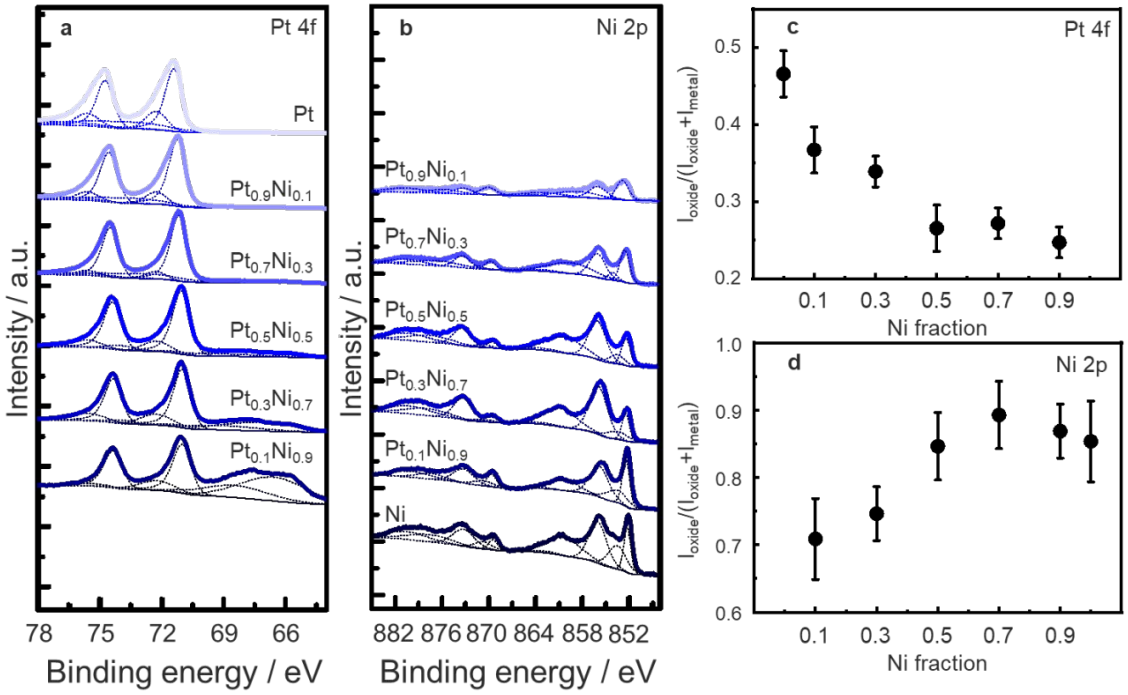

Figure 2. Pt 4f (a) and Ni 2p (b) XPS spectra of the Pt_xNi_{1-x} BCs on SiO_2 wafers from x = 0.9 to 0.1 as well as pure Pt and Ni clusters. The Pt 4f peaks of Pt $4f_{7/2}$ and Pt $4f_{5/2}$ are deconvoluted into Pt metal phase (71.1 eV and 74.4 eV) and Pt oxide phases (72.3 eV, 75.7 eV, 73.9 eV and 77.3 eV); the Pt 4f XPS intensity ratio of the oxide phase is summarized in (c). The Ni 2p peaks of Ni 2p3/2 and Ni 2p1/2 are deconvoluted into a Ni metal phase (852.5 eV and 869.6 eV) and Ni hydroxide/oxide phases (853.2 eV, 870.7 eV, 855.9 eV, 873.4 eV, 860.4 eV, 877.9 eV); the Ni 2p XPS intensity ratio of the oxide phase is summarized in (d).

The electronic structure and the nature of the phases occurring in the air exposed Pt_xNi_{1-x}/SiO_2 (x = 0, 0.1, 0.3, 0.5, 0.7, 0.9 and 1) samples were complementarily investigated by XPS. The composition and amount of the oxidized components can be revealed by deconvoluting the Pt 4f and Ni 2p peaks. The best fits of the high-resolution XPS core-level spectra in the Pt 4f and Ni 2p energy region, as well as the summary plots of Pt 4f and Ni 2p peaks with the different phases are presented in Figure 2. It is found that Pt atoms within the BCs mainly remained metallic and that a large fraction of Ni atoms was oxidized into Ni hydroxide/oxide after the samples were exposed to air. Furthermore, a composition dependent oxidation rate is observed. Pt 4f peaks can be deconvoluted into three sets of Pt $4f_{7/2}$ and Pt $4f_{5/2}$ peaks, corresponding to Pt metal (71.1 eV and 74.4 eV), PtO (72.3 eV and 75.7 eV) and PtO_2 phases (73.9 eV and 77.3 eV). Additionally, a broad peak that appears between 66 eV and 69 eV when the Ni fraction is above 0.5 can be assigned to convoluted Ni 3p peaks. The intensity evolution of these Ni 3p peaks is fully consistent with the BC composition.

Pure platinum and Pt-rich clusters feature a larger fraction of platinum oxides than their Ni-rich bimetallic counterparts. Pt oxides consist mostly of PtO with an additional contribution of the higher oxidation phase PtO_2 that is only present in the Pt rich BCs. In BCs with Ni fractions above 0.5, the Pt oxidation rate drops significantly. This observation is consistent with the STEM observation that Pt atoms are predominantly present in the BC core. This suggests that their oxidation is prevented by the Ni atoms forming the BC outer shell. Similarly, the oxidation state of the Ni atoms also varies with the BC composition. The Ni $2p_{3/2}$ and Ni $2p_{1/2}$ peaks can be deconvoluted into Ni metal (852.5 eV and 869.6 eV), NiO (853.2 eV and 870.7 eV), $Ni(OH)_2$ (855.9 eV and 873.4 eV) and NiOOH phases (860.4 eV and 877.9 eV). The peaks centred around 863.6 eV and 880.8 eV are assigned to the satellite peaks of Ni $2p_{3/2}$ and Ni $2p_{1/2}$. In Ni rich BCs, more than 70% of the Ni atoms are oxidized. Their average oxidation state tends to increase with the Ni fraction, reaching a maximum in $Pt_{0.3}Ni_{0.7}$ BCs. This can be attributed to the relative stability of the Ni oxide and hydroxide phases; previous studies have shown that the electronic structure of Ni is modified by neighbouring Pt atoms, favouring Ni oxidation when these atoms are present in the BC shell.[21, 22, 29] When the Ni fraction decreases below 0.5, the cluster structure consists of a Ni enriched core and a Pt enriched shell, resulting in a decrease in the Ni oxidation rate. XPS analysis of the deconvoluted Pt and Ni metal peaks in Pt_xNi_{1-x} BCs gives a clear indication of the electronic structural modification of Pt clusters upon mixing with Ni. The Pt metal 4f binding energy decreases from 71.3 eV to 71.1 eV while the Ni metal 2p binding energy increases from 852.1 eV to 852.6 eV,

compared to their respective monometallic counterparts. This binding energy change can be ascribed to a combined result of the charge transfer between the two elements, band modification by the neighbouring element, and the different oxide fractions within the BCs after air exposure.[54]

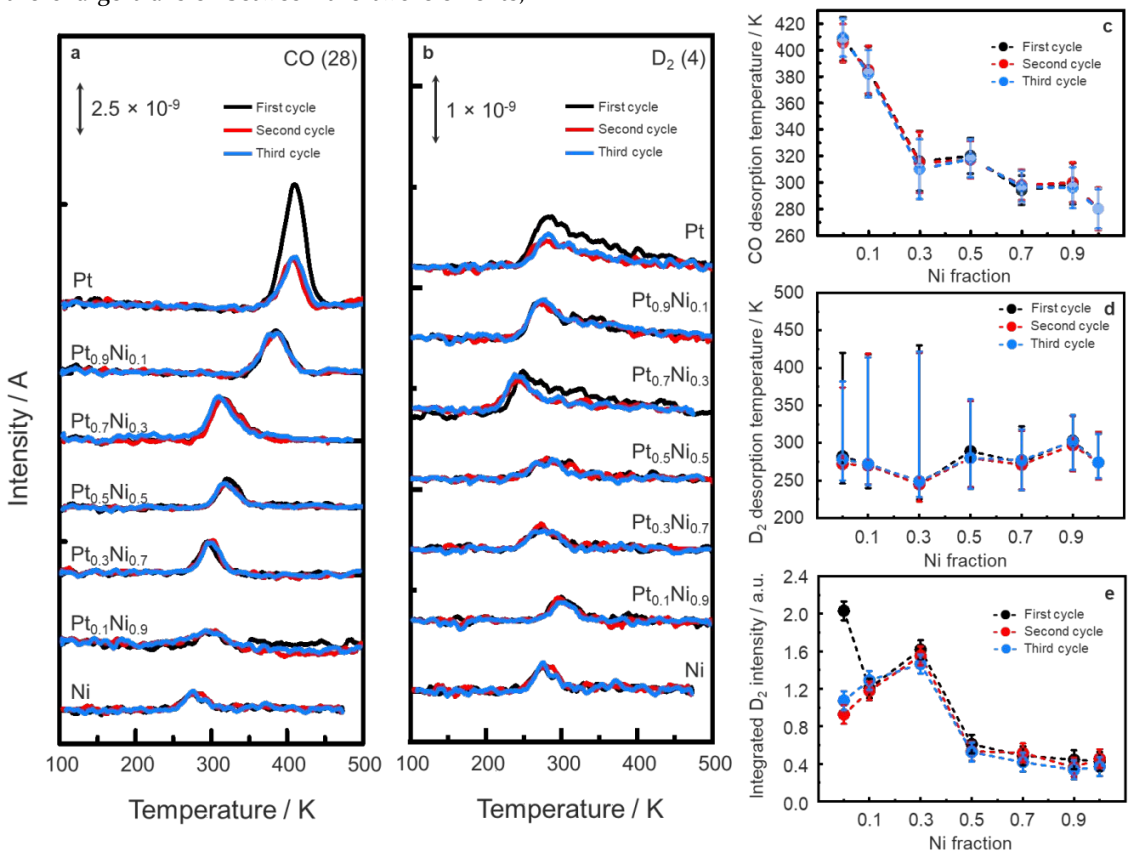

Figure 3. TPD traces of methanol decomposition on Pt_xNi_{1-x} BCs of different compositions on SiO_2 supports, showing the desorption of (a) CO and (b) D_2. Overviews of the (c) CO and (d) D_2 desorption temperature. The desorption peaks are indicated with the full circles, while the upper and lower limit of desorption are indicated with bars. (e) The integrated amount of desorbed D_2 as a function of the Ni fraction in the BCs.

CATALYTIC ACTIVITY OF PT_XNI_{1-X} CLUSTERS

The catalytic activity and stability of the Pt_xNi_{1-x} (x = 1, 0.9, 0.7, 0.5, 0.3, 0.1, 0) BCs deposited on SiO_2/Si wafers and without ambient exposure, were tested under UHV by TPD in the methanol dehydrogenation reaction, by ramping the temperature from 100 K to 500 K at a rate of 4 K/s in 3 reaction cycles. The amount of hydrogen desorption is directly related to the methanol dehydrogenation catalytic activity of the BCs, whereas the CO desorption temperature is correlated to the strength of the CO poisoning effect. (see SI for more details on TPD experiment and analysis procedures)

The TPD traces for CO and D_2 in three subsequent cycles of methanol decomposition are shown in Figure 3, together with the dependence on the Ni content of the CO desorption temperature and the amount of D_2 desorption. The exclusive detection of CO and D_2 in the quadrupole mass spectrometer (QMS) indicates that the dominant reaction within the investigated temperature range is methanol dehydrogenation (C-D bond scission) highlighting the excellent selectivity of Pt-Ni BCs. As the same activity is measured in subsequent reaction cycles while no CD_3 is formed, the C-O bond scission pathway that ultimately forms carbon deposits and poisons the catalyst surface can be safely excluded (Figure S5). From the amount of CO and D_2 desorption it is found that, except for monometallic Pt clusters, all BCs show a stable methanol dehydrogenation catalytic activity over the three reaction cycles. Although monometallic Pt clusters feature the highest activity of all samples in the first reaction cycle, their activity drops to a level similar to the other Pt-rich ($Pt_{0.9}Ni_{0.1}$ and $Pt_{0.7}Ni_{0.3}$) BCs after the first cycle. All Pt_xNi_{1-x} compositions have a single CO desorption feature.

The evolution of the CO desorption temperature, which is related to the strength of the CO poisoning effect shows a systematic 2-stage decrease when the Ni fraction increases (Figure 3-c). A fast decrease is observed for Ni fractions ranging from 0 to 0.3, while a slow one occurs for Ni fractions from 0.5 to 1. In BCs with a Ni fraction of 0.3, the CO poisoning effect is significantly reduced at room temperature by alloying Pt with Ni for the considered particle sizes. A low CO desorption temperature was observed in Ni rich BCs and pure Ni clusters. Since CO-Ni metal interactions are typically strong and expected to

result in a high CO desorption temperature of around 400 K,[56, 57] this strongly suggests that the Ni atoms on Ni-rich cluster surfaces have interacted with traces of O_2 molecules inside the UHV chambers, even though the samples were transferred via a UHV transport vessel.[58] We therefore conclude that in the Ni rich BCs and pure Ni clusters, the CO molecules are desorbed from a Ni oxide surface.

The methanol dehydrogenation catalytic activity, defined by the integrated intensity of D_2 peaks, is stable during the three TPD cycles for all Pt_xNi_{1-x} BCs as well as for the monometallic Ni clusters. The 50% reduction in the pure Pt clusters activity in the subsequent cycles may be assigned to the lower accessibility of the reaction sites on the cluster surface.[7] The variation of the D_2 desorption temperature versus the BC composition (Figure 3-d) shows a minimum at $Pt_{0.7}Ni_{0.3}$. D_2 desorbs in the 250-300 K range indicating that Ni alloyed Pt clusters are always catalytically active below room temperature. D_2 desorption also reveals the type of element present at the cluster surface. In Pt-rich BCs, the tail of the D_2 desorption feature extends even to 400 K, suggesting that D_2 molecules are formed and desorbed from the Pt surface,[59] while no desorption higher than 350 K is observed in Ni-rich BCs. This is possibly due to the presence of a Ni enriched shell at the surface.

A volcano-like plot relating the integrated intensity of D_2 desorption to the BC composition (Figure 3-e) peaking at the $Pt_{0.7}Ni_{0.3}$ composition (+ 60% activity relative to pure Pt clusters) is observed. As the BCs catalytic activity reflects their surface properties, the nearly plateau observed for Ni fractions of 0.5 and up to 1 (pure Ni clusters) suggests that in these BCs the same type of atoms are present at the surface. Considering the composition-tunable phase segregated atomic arrangement observed in these BCs, a majority of Ni atoms are likely forming the surface of the Ni rich BCs. Similarly, in BCs with Ni fractions of 0.1 and 0.3 the presence of a majority of Pt atoms is expected at the cluster surface. As Pt-Ni BCs tested under methanol decomposition were not exposed to air, the nature and amount of the oxide phases at the BC surface is expected to differ substantially from that of their air-exposed counterparts, determined by XPS. For Ni fractions of 0.5 and up to the pure Ni, only a superficial NiO layer is likely present at the cluster surface in line with the discussion above, while for BCs with Ni fractions of 0.1 and 0.3, Pt atoms at the surface are expected to be mostly in a metallic state. The absence of CO_2 signal in the TPD traces of methanol decomposition (see Figure S6) further substantiates that the surface of the most active $Pt_{0.7}Ni_{0.3}$ BC is free of Pt and/or Ni oxides that could have oxidized the formed CO species. $Pt_{0.7}Ni_{0.3}$ BCs, which showed the best catalytic performance combined with a reduced CO poisoning, was selected for further theoretical modelling of its electronic structure.

DFT CALCULATIONS OF PT_XNI_{1-X} CLUSTERS SURFACE AND ITS CO-PT INTERACTIONS

In order to understand the origin of the decreased CO desorption temperature in Ni alloyed Pt clusters, the electronic band structure was calculated for cluster sizes of about 2 nm and geometries in line with the observed structures in the STEM experiments. As Ni alloyed and pure Pt clusters tested for their catalytic activity in TPD were not exposed to air, non-oxidized Pt_{459}, Pt_{561}, $Pt_{353}Ni_{106}$ and $Pt_{417}Ni_{144}$ were selected as representative monometallic Pt clusters and $Pt_{0.7}Ni_{0.3}$ BCs under methanol dehydrogenation conditions. The precise sizes correspond to closed atomic shells in FCC particles that have either the Wulff shape with small (100) facets (the 459 atom clusters) or larger (100) facets (the 561 atom clusters). Geometric details of the constructed clusters can be found in Figures 4-a, 4-b and in the method section. To model the $Pt_{353}Ni_{106}$ BC, a first isomer was constructed with random Pt-Ni alloy core and Pt surface, motivated by the HAADF-STEM and TPD results. Alternative atomic orderings that were considered and locally optimized are two different fully random alloy clusters and a Ni-core/Pt-shell cluster. The locally optimized random core-Pt shell structure was found to have the lowest energy, followed by the Ni-core/Pt-shell (+15.1 eV higher in total energy or 32.9 meV / atom). The two random configurations are energetically the least favourable (+16.5 eV and +16.6 eV, or 35.9 meV/atom and 36.2 meV/atom, respectively). As the obtained lowest energy structure is consistent with the STEM experimental result in **Error! Reference source not found.**, further calculations were done with the random core-Pt shell BCs.

A rather simplified, however very successful, model used to understand the interaction of small molecules and metal surfaces is the d-band centre model, in which it is considered that on metal surfaces with a lower d-band centre (with respect to the Fermi level) adsorbates will bond less strongly.[22] In this model, it is considered that upon adsorption of a molecule on a metal surface, a bonding and an antibonding state are created, and the binding energy of the surface-molecule system will depend on the electron population of the adsorbate antibonding state that lies right above the metal d-band. The less populated the antibonding state is, the stronger is the adsorbate binding energy. This idea related the d-band centre of the metal surface to the adsorbate binding energy; surfaces with a lower d-band centre will have a higher electron population of the surface-molecule antibonding state, thus decreasing its binding energy.[60]

In the $Pt_{353}Ni_{106}$ cluster (Figure 4-a) we distinguish two types of surface Pt atoms, those with another Pt atom subsurface and those with a subsurface Ni atom where Pt atoms form a skin. In the calculations of the different Pt atoms, the d-band centre of the first type of Pt atoms is -2.51 ± 0.03 eV (with respect to the Fermi level), whereas it is -2.79 ± 0.03 eV for the second type. The range of the d-band centre corresponds to the different symmetry inequivalent Pt sites on the surface. The d-band centre averaged over all Pt atoms in $Pt_{353}Ni_{106}$ cluster is -2.65 eV compared to -2.35 ± 0.10 eV and -2.29 ± 0.12 eV in pure Pt_{459} and Pt_{561} clusters, respectively. The relative energy of the d-electrons is important for the CO binding and therefore, lowering the d-band centre of the metal should lead to a

lower CO binding strength. In order to verify this argument, we calculated binding energies of the CO molecules on various surface sites of the clusters. The correlation between the d-band centre and the CO binding energy (see Figure 4-c), shows that the behaviour found for the CO binding energy on various Pt sites on these four clusters is consistent with the d-

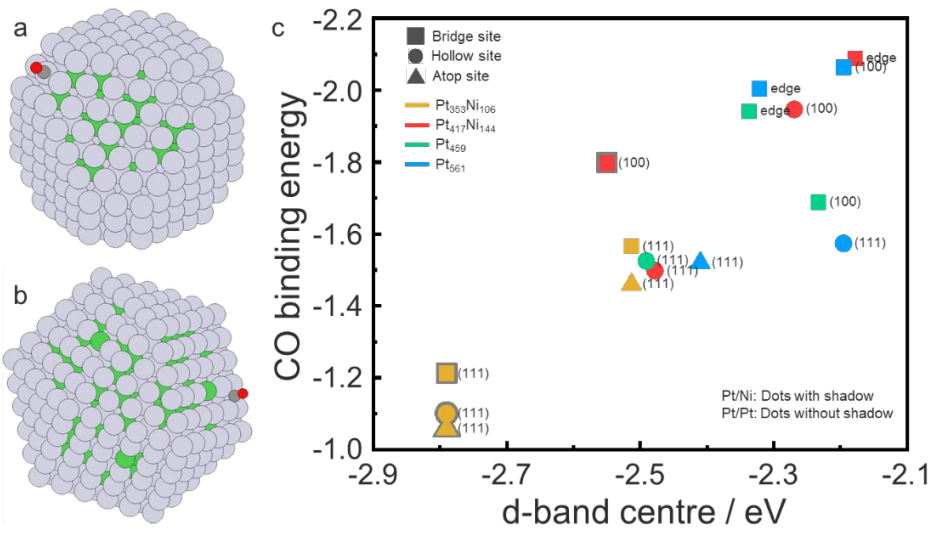

Figure 4. (a) Wulff constructed $Pt_{353}Ni_{106}$ clusters and (b) $Pt_{417}Ni_{144}$ clusters constructed with larger (100) surfaces. The CO binds on both clusters on a bridge site of a (100) Pt surface. The grey, green, dark grey, and red balls represent Pt, Ni, C, and O atoms, respectively. (c) Overview of the CO binding energy as a function of the d band centre of the Pt atom on which the CO is adsorbed, for Pt atoms at the edge, (100), (111) surfaces of the Wulff constructed $Pt_{353}Ni_{106}$ (orange) and larger (100) surface $Pt_{417}Ni_{144}$ (red) BCs with either Pt or Ni subsurface atoms, as well as Pt_{459} (green) and Pt_{561} (blue) clusters. The CO adsorption on bridge site, hollow site and atop sites are presented by squares, circles and triangles, respectively. The CO adsorption on the Pt atoms with Ni subsurface atoms are indicated with grey shadow.

band model. A detailed table of all the calculated CO binding energies on different surface sites with Ni or Pt atoms at the subsurface is presented in Table S1. Although DFT calculations were performed only on two ideal clusters, we are confident that the computations captured the main trend of CO adsorption. Subsurface Ni reduces the CO binding energy on Pt, whether it is located on the flat 111 or more open 100 surfaces as well as on the edge sites. Surface defects like vacancies or adatoms are expected to alter the absolute values of the CO binding energy but very unlikely modify the general trend of a reduced CO binding energy in presence of subsurface Ni atoms. The d-electron population analysis of the BCs also reveals a substantial modification of the electronic structure of skin Pt atoms by neighbouring subsurface Ni atoms. In particular, a Löwdin population analysis[61] shows a reduction of their d-electron population by nearby Ni atoms, which may be in line with the model proposed by Toda et al.[62] The correlation between d-electron population and CO binding energy is presented in Figure S7 and Table S2. In general, independently of whether the Pt atoms are located at (100) or (111) surfaces, or at edge sites, the CO binding energy is lower if a Ni atom is present at the subsurface. Therefore, the decreased CO desorption temperature on Pt_xNi_{1-x} BCs can be assigned to local modifications of the d-band electronic structure of surface Pt atoms forming a skin, induced by the presence of subsurface Ni, which results in a weakened CO-Pt interaction. This is in excellent agreement with the observed reduced CO desorption temperature with Ni fraction in the methanol decomposition TPD experiments.

A maximum in the methanol activity is reached for the same $Pt_{0.7}Ni_{0.3}$ cluster composition suggesting that it may be directly related to the CO poisoning of the clusters surfaces.[28, 63] Although our calculations show that the first methanol dissociation reaction intermediate $HOCH_2$ binds well to the Pt-skin surface of $Pt_{353}Ni_{106}$ clusters, the calculated methanol binding energy on the same cluster is almost site independent and has a small value of - 0.1 eV, compared to -0.33 eV for pure Pt(111).[64] This is in line with previous calculations that showed that downshifting the Pt d-band centre not only results in weakening the CO binding energy but also that of the methanol itself. As the dissociative adsorption of methanol involving a first-hydrogen extraction by O–H or C–H bond scission is regarded as the rate-determining step of methanol dehydrogenation on Pt surfaces, [64, 65] a reduced binding energy of methanol to Pt is not expected to favour its dissociation. [63] This suggests that the increased methanol activity observed for the x = 0.3 composition is more related to the reduction of the CO poisoning that blocks the available Pt active sites at the surface of the cluster rather than to an increase in the intrinsic methanol dehydrogenation activity in line with the reported 60% activity increase of $Pt_{0.7}$ $Ni_{0.3}$ BCs in comparison to Pt clusters. This would be in good agreement with previous

work that identified OH and CO binding free energies as the main descriptors of the methanol dehydrogenation on metal surfaces in DMFCs.[66] As the reaction was carried out in UHV, the enhanced methanol activity in this work is then expected to be mainly described by the CO binding free energy. Calculated CO desorption energies (E_d) from TPD experiments are in line with the CO binding energies computed by DFT, therefore confirming that our Pt-Ni catalysts dehydrogenate methanol selectively by forming exclusively CO and D_2, excluding the formation of CD_4 (See SI).

This Pt-skin with subsurface Ni architecture at the surface of 2 nm $Pt_{0.7}Ni_{0.3}$ BCs resembles closely those identified at the extended surfaces of Pt-Ni alloyed electrocatalysts as highly active surfaces for the ORR that occurs at the cathode of the MFC.[28] Interestingly, this specific Pt-skin surface architecture forms preferentially on electrodes with the similar Pt_3Ni composition corresponding to the most active BCs identified in this work.[28-31] The computed d-band shift of ca. -2.7 eV for the Pt skin on a Pt_3Ni alloy surface that corresponds to an optimal adsorption strength of the OH molecules in the ORR are in line with the corresponding value of -2.65 eV averaged over all Pt atoms and -2.8 eV for the (111) facet sites of $Pt_{353}Ni_{106}$ BCs calculated in this work.[28] The corresponding d-band shift of -2.5 eV for the extended surfaces of pure Pt[28] is also in line with the values of -2.5 eV computed here for the (111) facet sites of pure Pt_{561} and Pt_{459}, as well as the Pt surface atoms with Pt subsurface in $Pt_{353}Ni_{106}$ and $Pt_{417}Ni_{144}$ clusters. This demonstrates that thermodynamically stable highly catalytic active Pt skin architectures can be created on the nanoscale surfaces of small BCs with the CBD technology. This is achieved by tuning the BC composition to Pt_3Ni and taking advantage of the composition-dependent segregation profile resulting from the BCs nucleation mechanism, likely to be applicable to a variety of binary systems besides Pt–Ni.[28]

These results also suggest that the Pt-skin architecture that forms at the surface of $Pt_{0.7}Ni_{0.3}$ clusters feature not only an enhanced catalytic activity in the methanol dehydrogenation (+ 60% relative to pure Pt clusters) at the anode, but also in the ORR occurring at the cathode of the MFCs. As for the ORR, the relationship between the specific methanol dehydrogenation activity and the d-band centre position on the Pt-skin surfaces exhibits a volcano-like shape. The relative methanol dehydrogenation activity of $Pt_{0.9}Ni_{0.1}$ BCs (+20% relative to pure Pt clusters) suggests the formation of a Pt-surface with a Pt subsurface configuration with an estimated d-centre downshift of -2.5 eV, while for $Pt_{0.5}Ni_{0.5}$, $Pt_{0.3}Ni_{0.7}$, $Pt_{0.1}Ni_{0.9}$ BCs showed a reduced activity (-50 to -60% relative to pure Pt clusters) due to the presence of an increasing amount of Ni oxide at their surfaces. As Pt-skins stable under (electro)chemical conditions[28, 34] can be generally obtained by a simple mild annealing of bimetallic Pt_3Ni (nano)structures,[28, 32] we expect that the more oxidised surfaces of air-exposed Pt_3Ni BCs measured by XPS can be easily transformed into a stable Pt-skin architecture similar to that obtained in UHV after the same treatment.

CBD fabrication that enables a precise tuning of the electronic properties of bi-(multi-) metallic nanoparticles, may allow the emergence of a new generation of bi-(multi-) metallic systems with nanoscale-engineered well-defined Pt skin surfaces. These Pt-based (electro) catalysts with reduced Pt content show an enhanced catalytic activity in anode-related methanol dehydrogenation as well as in the cathode ORR, and therefore, can contribute to lowering the Pt loadings in polymer electrolyte membrane fuel cells and facilitate their utilisation as sustainable and clean energy conversion devices.

CONCLUSIONS

The atomic arrangement and the catalytic activity of 2.0 nm gas phase Pt_xNi_{1-x} BCs deposited on TEM grids and SiO_2 supports were experimentally studied by HAADF-STEM, XPS and TPD. HAADF-STEM showed that these BCs have composition-tunable atomic arrangements with minority element enriched core and majority element dominated shell structure, most likely stemming from their nucleation mechanism. The BCs oxidation and phase composition revealed by XPS confirmed their phase-segregated structure. TPD under UHV conditions show that methanol dehydrogenation via C-D and O-D bond scission occurs on the cluster surface, with CO and D_2 as products. A volcano-like methanol dehydrogenation catalytic activity, triggered by a strong reduction of CO poisoning effect, is obtained by alloying Pt with Ni and peaks at the $Pt_{0.7}Ni_{0.3}$ composition. This is attributed by DFT calculations to a Pt-skin with subsurface Ni, where the local modifications of the Pt d-band, induced by Ni, leads to a high methanol dehydrogenation activity and weakened Pt-CO interaction, in agreement with the d-band centre model. We demonstrate a clear composition-tuned catalytic activity and CO poisoning effect of Pt-Ni BCs in the methanol decomposition reaction, explained by a composition-tuned segregation profile resulting directly from the BC nucleation mechanism. Tuning the BCs surface architecture to obtain a Pt-skin with subsurface Ni atoms, using the size and composition precision of the CBD fabrication, offers a new direction to designing long lifetime and highly active methanol fuel cell Pt-based anode but also cathode catalysts.

METHODS/EXPERIMENTAL DETAILS

Production of Pt_xNi_{1-x} clusters. Composition controlled Pt_xNi_{1-x} (x = 0, 0.1, 0.3, 0.5, 0.7, 0.9, 1) BCs were produced by a combination of pulsed laser (10 Hz, Nd:YAG lasers) ablation of Pt_xNi_{1-x} (ACI alloy, purity 99.5%) plate targets and inert gas (He, purity 99.9999%) condensation.[51] The size distribution of the BCs was monitored by reflectron time-of-flight (RTOF) mass spectrometry and optimized to have an average size around 2.0 ± 1.4 nm. Following a supersonic expansion into vacuum, the molecular beam of Pt_xNi_{1-x} BCs was guided to the deposition chamber and soft-landed (~ 500 m/s) on TEM grids and on SiO_2/Si (100) substrates, for STEM and TPD

measurements, respectively.[67] The substrates were held at room temperature and equivalent atomic coverages of 1 ML for TEM and 5ML for TPD were deposited. Assuming the cluster diameter is 2 nm, the projected area coverage of 1 ML and 5 ML will be around 5 % and 25 %, respectively. The flux of the BCs was monitored by a quartz crystal microbalance and the BC coverage was controlled by the deposition time assuming a constant cluster flux.

Structures of the Pt_xNi_{1-x} clusters and atomic arrangements. Atomic resolution STEM imaging was performed by a FEI Titan G2 80-200 Chemi-STEM operating at 200 keV and equipped with spherical aberration (Cs) probe corrector, as well as a high-angle annular dark-field (HAADF) detector. The cluster size distributions of the Pt_xNi_{1-x} BCs were measured with low magnification in a sample of more than 300 BCs. The cluster size was determined by measuring the diameter cross-section of individual clusters. Identification of a possible core-shell structure was obtained by the Z-contrast of HAADF-STEM (Z is the elemental atomic number). The HAADF-STEM intensity is proportional to $Z^{1.5}$ with the camera length employed.[53] The large difference of the atomic number between Pt and Ni (Z_{Pt} = 78; Z_{Ni} = 28) allows distinguishing the elemental atomic arrangement within the clusters directly from the HAADF-STEM image intensity contrast. STEM image analysis was carried out with the imageJ Fiji software. The intensity profile of each cluster was obtained by first identifying the position of the centre through averaging, and then binning the intensity in polar coordinates as a function of the radial distance to the centre.

Methanol decomposition on $Pt_xNi_{1-x}/SiO_2/Si$ (100). Boron doped amorphous SiO_2/Si(100) wafers were heated up with direct resistive heating and cleaned more than three times by a flash-heating process to 700 K to desorb all contaminations in an UHV chamber (base pressure 6×10^{-10} mbar) dedicated to the TPD experiments. The desorbed contaminations were monitored by a quadruple mass spectrometer (QMS), considering the masses of H_2O (18), CO/N_2 (28), O_2 (32), Ar (40), CO_2 (44). The sample cleaning process was terminated at the point the signal of the listed masses was reduced to the noise level. The methanol-d4 (CD_3OD) was purified in an UHV compatible glass test tube by repeated freeze–pump–thaw cycles to remove all the gases in the test tube and the vacuum gas lines. The methanol-d4 was introduced into the UHV chamber by a leak valve and was guided to the sample surface by a dozer tube. The cleaned SiO_2 sample was exposed to 5 L of methanol-d4 at 100 K. The methanol-d4 desorption was conducted with PID controlled linear heating using a 4 K/s ramping rate and the molecule desorption was monitored by the QMS considering all possible cracking patterns. No C-H, C-O and O-H bond scission was observed on the clean SiO_2 surface.

The cleaned SiO_2/Si (100) samples were then transferred in a home-built UHV transport vessel with base pressure in the 10^{-10} mbar range to the CBD chamber with base pressure in the 10^{-9} mbar range. After deposition of the Pt_xNi_{1-x} BCs on the SiO_2/Si (100) substrates, the samples were transferred back to the TPD setup for methanol decomposition experiments. The samples were cooled down to 100 K by a flow of liquid nitrogen (LN_2) in flexible stainless steel tubes and exposed to 5 L methanol-d4 for saturation adsorption of methanol-d4 on the surface. TPD spectra were taken in the 100 K to 500 K temperature range using a 4 K/s ramping rate. The catalytic experiments were repeated 3 times for each same sample to characterize the stability and catalytic activity.

Electronic structure and oxidation state characterizations. XPS experiments were performed at room temperature and under UHV conditions (base pressure 1.6×10^{-9} mbar), but after exposure of the samples to air, in a Kratos Axis Supra system with a monochromatized Al Kα X-ray source (1486.6 eV) operated at 10 mA. The spectra were collected by hemispherical analyser with passing energy of 160 eV and 20 eV for the wide scan and high-resolution spectra, respectively. The spectra were aligned to the adventitious carbon peak C 1s at 284.8 eV. The deconvolution and fitting of the peaks was done with CasaXPS software.[68] The following spin-orbit coupling constraints were considered: peak separations of 17.3 eV and 3.35 eV and peak area ratios of 2/3 and 3/4 for Ni 2p and Pt 4f, respectively.

DFT calculations on the electronic structures and CO / methanol - Pt interactions. The Pt_{459}, Pt_{561}, $Pt_{353}Ni_{106}$ and $Pt_{417}Ni_{144}$ clusters were modelled by density functional theory (DFT) with the CP2K code.[69-71] The BLYP functional with GTH pseudopotentials[72] (18 active electrons) was used for both Ni and Pt. The DZVP-MOLOPT-SR basis was employed. The 459- and 561-atom clusters were placed in cubes with edge sizes of 29 Å side and 27 Å, respectively. Both the local atomic structure and total spin were optimized. The diagonalization method with the Kerker mixing was used in the electronic structure optimization. The charge decomposition analysis was performed using the Hirshfeld,[73] Bader, Löwdin, and Mulliken methods. The charge decomposition analysis is shown in Table S3. Two different type of random core-Pt shell clusters were constructed. The Wulff constructed $Pt_{353}Ni_{106}$ cluster (diameter ca. 2.4 nm) was modelled with Pt surface tensions of 1.49 J/m² for (111) and 1.81 J/m² for (100) from Ref S1. (Figure 4-a). This lead to very small (100) facets of only four atoms. $Pt_{417}Ni_{144}$ cluster (diameter ca. 2.7 nm) was generated with larger (100) facets (Figure 4-b). Pure Pt cluster has a slightly higher energy, namely 4.5 meV/atom.

ASSOCIATED CONTENT

The **Supporting Information** is available free of charge on the ACS Publications website at DOI: 10.1021/acs.chemmater.xxxxx. It contains Figures S1 to S7, Tables S1 to S3 and Additional material including a comparison of the preparation and structures of Au-Ag BCs with Pt-Ni BCs, the TPD experiment and analysis procedures and details on the DFT calculations.

AUTHOR INFORMATION

Corresponding Authors

* Ting-Wei Liao: tiwei@dtu.dk

* Didier Grandjean: didier.grandjean@kuleuven.be
* Peter Lievens: peter.lievens@kuleuven.be

Present Addresses

† Section for Surface Physics and Catalysis, Department of Physics, Technical University of Denmark, 2800 Kgs Lyngby, Denmark

Author Contributions

‡T.-W. L and A.Y. contributed equally to this manuscript. P. L., E. J., D. G., A. Y. and T.-W. L. designed the project. K.-J. H and T.-W. L. designed, constructed, and studied the reactivity in the TPD setup. A. Y., Y. N. and T.-W. L. synthesized and deposited bimetallic clusters. X.-K. W., M. H., R. E. D.-B. carried out the STEM measurements. J. V. and R. E. P. carried out the XPS measurements. P. F. and K. L. performed the DFT calculations. All authors contributed to editing and proofreading of the manuscript.

Notes

The authors declare no competing financial interests.

ACKNOWLEDGMENT

The research leading to these results has received funding from the European Union's Seventh Framework Programme (FP7/2007-2013) under grant agreement No. 607417 (Catsense project). P.F. acknowledges the FWO for a postdoctoral grant. A.Y. and E.J. acknowledge the KU Leuven Research Council (CELSA/18/032). The Swansea team would like to acknowledge the assistance provided by Swansea University College of Engineering AIM Facility, which was funded in part by the EPSRC (EP/M028267/1), the European Regional Development Fund through the Welsh Government (80708) and the Ser Solar project via Welsh Government. The Swansea team, K.L., X.-K.W., M.H. and R.E.D.-B. acknowledge the European Union's Horizon 2020 Research and Innovation Program under grant agreement No. 686053 (CritCat Project).

REFERENCES

(1) Olah, G. A., Beyond Oil and Gas: The Methanol Economy. *Angew. Chem. Int. Ed.* **2005,** *44* (18), 2636-2639.

(2) Gumber, S.; Gurumoorthy, A. V. P., Chapter 25 - Methanol Economy Versus Hydrogen Economy A2 - Basile, Angelo. In *Methanol*, Dalena, F., Ed. Elsevier: Amsterdam, Netherlands, 2018; Chapter 25, pp 661-674.

(3) Hung, T.-C.; Liao, T.-W.; Liao, Z.-H.; Hsu, P.-W.; Cai, P.-Y.; Lee, H.; Lai, Y.-L.; Hsu, Y.-J.; Chen, H.-Y.; Wang, J.-H.; Luo, M.-F., Dependence on Size of Supported Rh Nanoclusters in the Decomposition of Methanol. *ACS Catal.* **2015,** *5* (7), 4276-4287.

(4) Rostrup-Nielsen, J. R.; Nielsen, R., Fuels and Energy for the Future: The Role of Catalysis. *Catal. Rev.* **2004,** *46* (3-4), 247-270.

(5) Debe, M. K., Electrocatalyst Approaches and Challenges for Automotive Fuel Cells. *Nature* **2012,** *486* (7401), 43-51.

(6) Chao, C.-S.; Liao, T.-W.; Wang, C.-X.; Li, Y.-D.; Hung, T.-C.; Luo, M.-F., Obstruction by CO of the Decomposition of Methanol on Pt Nanoclusters on a Thin Film of Al2O3/NiAl(100). *Appl. Surf. Sci.* **2014,** *293*, 352-358.

(7) Chao, C.-S.; Li, Y.-D.; Liao, T.-W.; Hung, T.-C.; Luo, M.-F., Decomposition of Methanol on Partially Alumina-Encapsulated Pt Nanoclusters Supported on Thin Film Al2O3/NiAl(100). *Appl. Surf. Sci.* **2014,** *311*, 763-769.

(8) Glüsen, A.; Dionigi, F.; Paciok, P.; Heggen, M.; Müller, M.; Gan, L.; Strasser, P.; Dunin-Borkowski, R. E.; Stolten, D., Dealloyed PtNi-Core–Shell Nanocatalysts Enable Significant Lowering of Pt Electrode Content in Direct Methanol Fuel Cells. *ACS Catal.*. **2019**, 3764-3772.

(9) Ehteshami, S. M. M.; Chan, S. H., A Review of ElectroCatalysts with Enhanced CO Tolerance and Stability for Polymer Electrolyte Membarane Fuel Cells. *Electrochim. Acta* **2013,** *93*, 334-345.

(10) Baschuk, J. J.; Li, X. G., Carbon Monoxide Poisoning of Proton Exchange Membrane Fuel Cells. *Int. J. Energ. Res.* **2001,** *25* (8), 695-713.

(11) Liu, J. L.; Lucci, F. R.; Yang, M.; Lee, S.; Marcinkowski, M. D.; Therrien, A. J.; Williams, C. T.; Sykes, E. C. H.; Flytzani-Stephanopoulos, M., Tackling CO Poisoning with Single-Atom Alloy Catalysts. *J. Am. Chem. Soc.* **2016,** *138* (20), 6396-6399.

(12) Kizhakevariam, N.; Stuve, E. M., Promotion and Poisoning of the Reaction of Methanol on Clean and Modified Platinum (100). *Surf. Sci.* **1993,** *286* (3), 246-260.

(13) Kramer, Z. C.; Gu, X. K.; Zhou, D. D. Y.; Li, W. X.; Skodje, R. T., Following Molecules through Reactive Networks: Surface Catalyzed Decomposition of Methanol on Pd(111), Pt(111), and Ni(111). *J. Phys. Chem. C* **2014,** *118* (23), 12364-12383.

(14) Sexton, B. A., Methanol Decomposition on Platinum (111). *Surf. Sci.* **1981,** *102* (1), 271-281.

(15) Stottlemyer, A. L.; Ren, H.; Chen, J. G., Reactions of Methanol and Ethylene Glycol on Ni/Pt: Bridging the Materials Gap between Single Crystal and Polycrystalline Bimetallic Surfaces. *Surf. Sci.* **2009,** *603* (16), 2630-2638.

(16) Feng, Y. Y.; Bi, L. X.; Liu, Z. H.; Kong, D. S.; Yu, Z. Y., Significantly Enhanced Electrocatalytic Activity for Methanol Electro-Oxidation on Ag Oxide-Promoted PtAg/C Catalysts in Alkaline Electrolyte. *J. Catal.* **2012,** *290*, 18-25.

(17) Hu, J. E.; Liu, Z. F.; Eichhorn, B. W.; Jackson, G. S., CO Tolerance of Nano-Architectured Pt-Mo Anode Electrocatalysts for PEM Fuel Cells. *Int. J. Hydrogen Energy* **2012,** *37* (15), 11268-11275.

(18) Kim, J. H.; Choi, S. M.; Nam, S. H.; Seo, M. H.; Choi, S. H.; Kim, W. B., Influence of Sn Content on PtSn/C Catalysts for Electrooxidation of C-1-C-3 Alcohols: Synthesis, Characterization, and Electrocatalytic Activity. *Appl. Catal., B* **2008,** *82* (1-2), 89-102.

(19) Rocha, T. A.; Ibanhi, F.; Colmati, F.; Linares, J. J.; Paganin, V. A.; Gonzalez, E. R., Nb as an Influential Element for Increasing the CO Tolerance of PEMFC Catalysts. *J. Appl. Electrochem.* **2013,** *43* (8), 817-827.

(20) Liao, M. S.; Cabrera, C. R.; Ishikawa, Y., A Theoretical Study of CO Adsorption on Pt, Ru and Pt-M (M = Ru, Sn, Ge) Clusters. *Surf. Sci.* **2000,** *445* (2-3), 267-282.

(21) Kitchin, J. R.; Norskov, J. K.; Barteau, M. A.; Chen, J. G., Modification of the Surface Electronic and Chemical Properties of Pt(111) by Subsurface 3d Transition Metals. *J. Chem. Phys.* **2004,** *120* (21), 10240-10246.

(22) Norskov, J. K.; Abild-Pedersen, F.; Studt, F.; Bligaard, T., Density Functional Theory in Surface Chemistry and Catalysis. *Proc. Natl. Acad. Sci. U.S.A.* **2011,** *108* (3), 937-943.

(23) Skoplyak, O.; Menning, C. A.; Barteau, M. A.; Chen, J. G. G., Experimental and Theoretical Study of Reactivity Trends for Methanol on Co/Pt(111) and Ni/Pt(111) Bimetallic Surfaces. *J. Chem. Phys.* **2007,** *127* (11).

(24) Garcia-Muelas, R.; Li, Q.; Lopez, N., Density Functional Theory Comparison of Methanol Decomposition and Reverse Reactions on Metal Surfaces. *ACS Catal.* **2015,** *5* (2), 1027-1036.

(25) Guo, W. L.; Tian, W. Q.; Lian, X.; Liu, F. L.; Zhou, M.; Xiao, P.; Zhang, Y. H., A Comparison of the Dominant Pathways for the Methanol Dehydrogenation to CO on Pt7 and Pt7-xNix (x=1, 2, 3) Bimetallic Clusters: A DFT Study. *Comput. Theor. Chem.* **2014,** *1032*, 73-83.

(26) Ferrari, P.; Molina, L. M.; Kaydashev, V. E.; Alonso, J. A.; Lievens, P.; Janssens, E., Controlling the Adsorption of Carbon

Monoxide on Platinum Clusters by Dopant-Induced Electronic Structure Modification. *Angew. Chem., Int. Ed.* **2016,** *55* (37), 11059-11063.

(27) Ferrari, P.; Vanbuel, J.; Tam, N. M.; Nguyen, M. T.; Gewinner, S.; Schollkopf, W.; Fielicke, A.; Janssens, E., Effects of Charge Transfer on the Adsorption of CO on Small Molybdenum-Doped Platinum Clusters. *Chem. - Eur. J.* **2017,** *23* (17), 4120-4127.

(28) Stamenkovic, V. R.; Mun, B. S.; Arenz, M.; Mayrhofer, K. J. J.; Lucas, C. A.; Wang, G. F.; Ross, P. N.; Markovic, N. M., Trends in Electrocatalysis on Extended and Nanoscale Pt-Bimetallic Alloy Surfaces. *Nat. Mater.* **2007,** *6* (3), 241-247.

(29) Stamenkovic, V. R.; Fowler, B.; Mun, B. S.; Wang, G. F.; Ross, P. N.; Lucas, C. A.; Markovic, N. M., Improved Oxygen Reduction Activity on Pt3Ni(111) via Increased Surface Site Availability. *Science* **2007,** *315* (5811), 493-497.

(30) Stamenkovic, V.; Mun, B. S.; Mayrhofer, K. J. J.; Ross, P. N.; Markovic, N. M.; Rossmeisl, J.; Greeley, J.; Norskov, J. K., Changing the Activity of Electrocatalysts for Oxygen Reduction by Tuning the Surface Electronic Structure. *Angew. Chem., Int. Ed.* **2006,** *45* (18), 2897-2901.

(31) Huang, J.-F.; Tseng, P.-K., High Performance Layer-by-Layer Pt3Ni(Pt-Skin)-Modified Pd/C for the Oxygen Reduction Reaction. *Chem. Sci.* **2018,** *9* (28), 6134-6142.

(32) Becknell, N.; Kang, Y.; Chen, C.; Resasco, J.; Kornienko, N.; Guo, J.; Markovic, N. M.; Somorjai, G. A.; Stamenkovic, V. R.; Yang, P., Atomic Structure of Pt3Ni Nanoframe Electrocatalysts by in Situ X-ray Absorption Spectroscopy. *J. Am. Chem. Soc.* **2015,** *137* (50), 15817-15824.

(33) Zhang, B.-W.; Zhang, Z.-C.; Liao, H.-G.; Gong, Y.; Gu, L.; Qu, X.-M.; You, L.-X.; Liu, S.; Huang, L.; Tian, X.-C.; Huang, R.; Zhu, F.-C.; Liu, T.; Jiang, Y.-X.; Zhou, Z.-Y.; Sun, S.-G., Tuning Pt-Skin to Ni-Rich Surface of Pt3Ni Catalysts Supported on Porous Carbon for Enhanced Oxygen Reduction Reaction and Formic Electro-Oxidation. *Nano Energy* **2016,** *19*, 198-209.

(34) Liu, J.; Lan, J.; Yang, L.; Wang, F.; Yin, J., PtM (M = Fe, Co, Ni) Bimetallic Nanoclusters as Active, Methanol-Tolerant, and Stable Catalysts toward the Oxygen Reduction Reaction. *ACS Sustainable Chem. Eng.* **2019,** *7* (7), 6541-6549.

(35) Liang, G. F.; He, L. M.; Arai, M.; Zhao, F. Y., The Pt-Enriched PtNi Alloy Surface and its Excellent Catalytic Performance in Hydrolytic Hydrogenation of Cellulose. *ChemSusChem* **2014,** *7* (5), 1415-1421.

(36) Jia, Q. Y.; Segre, C. U.; Ramaker, D.; Caldwell, K.; Trahan, M.; Mukerjee, S., Structure-Property-Activity Correlations of Pt-Bimetallic Nanoparticles: A Theoretical Study. *Electrochim. Acta* **2013,** *88*, 604-613.

(37) Dutta, A.; Ouyang, J. Y., Ternary NiAuPt Nanoparticles on Reduced Graphene Oxide as Catalysts toward the Electrochemical Oxidation Reaction of Ethanol. *ACS Catal.* **2015,** *5* (2), 1371-1380.

(38) Mu, R. T.; Fu, Q. A.; Xu, H.; Zhang, H. I.; Huang, Y. Y.; Jiang, Z.; Zhang, S. O.; Tan, D. L.; Bao, X. H., Synergetic Effect of Surface and Subsurface Ni Species at Pt-Ni Bimetallic Catalysts for CO Oxidation. *J. Am. Chem. Soc.* **2011,** *133* (6), 1978-1986.

(39) Park, K. W.; Choi, J. H.; Kwon, B. K.; Lee, S. A.; Sung, Y. E.; Ha, H. Y.; Hong, S. A.; Kim, H.; Wieckowski, A., Chemical and Electronic Effects of Ni in Pt/Ni and Pt/Ru/Ni Alloy Nanoparticles in Methanol Electrooxidation. *J. Phys. Chem. B* **2002,** *106* (8), 1869-1877.

(40) Wang, L. L.; Zhang, D. F.; Guo, L., Phase-Segregated Pt-Ni Chain-Like Nanohybrids with High Electrocatalytic Activity towards Methanol Oxidation Reaction. *Nanoscale* **2014,** *6* (9), 4635-4641.

(41) Huttel, Y., *Gas-Phase Synthesis of Nanoparticles*. John Wiley & Sons: Weinheim Germany, 2017.

(42) Ferrari, P.; Vanbuel, J.; Li, Y.; Liao, T.-W.; Janssens, E.; Lievens, P., The Double-Laser Ablation Source Approach. In *Gas-Phase Synthesis of Nanoparticles*, Wiley-VCH Verlag GmbH & Co. KGaA: Weinheim Germany, 2017; Chapter 4, pp 59-78.

(43) Liao, T.-W.; Yadav, A.; Hu, K.-J.; van der Tol, J.; Cosentino, S.; D'Acapito, F.; Palmer, R. E.; Lenardi, C.; Ferrando, R.; Grandjean, D.; Lievens, P., Unravelling the Nucleation Mechanism of Bimetallic Nanoparticles with Composition-Tunable Core-Shell Arrangement. *Nanoscale* **2018,** *10* (14), 6684-6694.

(44) Liao, T.-W.; Verbruggen, S. W.; Claes, N.; Yadav, A.; Grandjean, D.; Bals, S.; Lievens, P., TiO2 Films Modified with Au Nanoclusters as Self-Cleaning Surfaces under Visible Light. *Nanomaterials-Basel* **2018,** *8* (1).

(45) Vajda, S.; White, M. G., Catalysis Applications of Size-Selected Cluster Deposition. *ACS Catal.* **2015,** *5* (12), 7152-7176.

(46) Sun, S. H.; Murray, C. B.; Weller, D.; Folks, L.; Moser, A., Monodisperse FePt Nanoparticles and Ferromagnetic FePt Nanocrystal Superlattices. *Science* **2000,** *287* (5460), 1989-1992.

(47) Cha, S. K.; Mun, J. H.; Chang, T.; Kim, S. Y.; Kim, J. Y.; Jin, H. M.; Lee, J. Y.; Shin, J.; Kim, K. H.; Kim, S. O., Au-Ag Core-Shell Nanoparticle Array by Block Copolymer Lithography for Synergistic Broadband Plasmonic Properties. *ACS Nano* **2015,** *9* (5), 5536-5543.

(48) Benkó, T.; Beck, A.; Frey, K.; Srankó, D. F.; Geszti, O.; Sáfrán, G.; Maróti, B.; Schay, Z., Bimetallic Ag–Au/SiO2 Catalysts: Formation, Structure and Synergistic Activity in Glucose Oxidation. *Appl. Catal., A* **2014,** *479*, 103-111.

(49) Haldar, K. K.; Kundu, S.; Patra, A., Core-Size-Dependent Catalytic Properties of Bimetallic Au/Ag Core–Shell Nanoparticles. *ACS Appl. Mater. Interfaces* **2014,** *6* (24), 21946-21953.

(50) Escalera-López, D.; Niu, Y.; Park, S. J.; Isaacs, M.; Wilson, K.; Palmer, R. E.; Rees, N. V., Hydrogen Evolution Enhancement of Ultra-Low Loading, Size-Selected Molybdenum Sulfide Nanoclusters by Sulfur Enrichment. *Appl. Catal., B* **2018,** *235*, 84-91.

(51) Duncan, M. A., Invited Review Article: Laser Vaporization Cluster Sources. *Rev. Sci. Instrum.* **2012,** *83* (4).

(52) Geerts, L.; Cosentino, S.; Liao, T.-W.; Yadav, A.; Lin, P.-C.; Zharinov, V. S.; Hu, K.-J.; Longo, A.; Pereira, L. M. C.; Grandjean, D.; Rongé, J.; Lievens, P.; Martens, J. A., Highly Active Oxygen Evolution Reaction Model Electrode Based on Supported Gas-Phase NiFe Clusters. *Catal. Today* **2019**, 334, 59-67.

(53) Wang, Z.; Palmer, R., Intensity Calibration and Atomic Imaging of Size-Selected Au and Pd Clusters in Aberration-Corrected HAADF-STEM. *J. Phys.: Conf. Ser.* **2012,** *371* (1), 012010.

(54) Choi, E.; Oh, S. J.; Choi, M., Charge-Transfer in NixPt1-x Alloys Studied by X-Ray Photoelectron-Spectroscopy. *Phys. Rev. B* **1991,** *43* (8), 6360-6368.

(55) Li, Z.; Chen, H. Y. T.; Schouteden, K.; Picot, T.; Houben, K.; Liao, T.-W.; Van Haesendonck, C.; Pacchioni, G.; Lievens, P.; Janssens, E., Size-Dependent Penetration of Gold Nanoclusters through a Defect-Free, Nonporous NaCl Membrane. *Nano Lett.* **2016,** *16* (5), 3063-3070.

(56) Wu, F. L.; Huang, D. L.; Yue, Y.; Liu, L., Template Growth of Au, Ni and Ni-Au Nanoclusters on Hexagonal Boron Nitride/Rh(111): A Combined STM, TPD and AES Study. *RSC Adv.* **2017,** *7* (70), 44169-44177.

(57) Netzer, F. P.; Madey, T. E., The Structure of Co on Ni(111). *J. Chem. Phys.* **1982,** *76* (1), 710-715.

(58) Conrad, H.; Ertl, G.; Kuppers, J.; Latta, E. E., Adsorption of Co on Clean and Oxygen Covered Ni(111) Surfaces. *Surf. Sci.* **1976,** *57* (2), 475-484.

(59) Li, Y.-D.; Liao, T.-W.; Wang, C.-X.; Chao, C.-S.; Hung, T.-C.; Ho, C.-Y.; Luo, M.-F.; Lai, Y.-L.; Hsu, Y.-J., The Decomposition of Methanol on Au-Pt Bimetallic Clusters Supported by a Thin Film of Al2O3/NiAl(100). *RSC Adv.* **2014,** *4* (60), 31602-31613.

(60) Hammer, B.; Morikawa, Y.; Norskov, J. K., CO Chemisorption at Metal Surfaces and Overlayers. *Phys. Rev. Lett.* **1996,** *76* (12), 2141-2144.

(61) Löwdin, P. O., On the Non-Orthogonality Problem Connected with the Use of Atomic Wave Functions in the Theory of Molecules and Crystals. *J. Chem. Phys.* **1950,** *18* (3), 365-375.

(62) Toda, T.; Igarashi, H.; Uchida, H.; Watanabe, M., Enhancement of the Electroreduction of Oxygen on Pt Alloys with Fe, Ni, and Co. *J. Electrochem. Soc.* **1999,** *146* (10), 3750-3756.

(63) Kang, J.; Nam, S.; Oh, Y.; Choi, H.; Wi, S.; Lee, B.; Hwang, T.; Hong, S.; Park, B., Electronic Effect in Methanol Dehydrogenation on Pt Surfaces: Potential Control during Methanol Electrooxidation. *J. Phys. Chem. Lett.* **2013,** *4* (17), 2931-2936.

(64) Greeley, J.; Mavrikakis, M., Competitive Paths for Methanol Decomposition on Pt(111). *J. Am. Chem. Soc.* **2004,** *126* (12), 3910-3919.

(65) Ferrin, P.; Mavrikakis, M., Structure Sensitivity of Methanol Electrooxidation on Transition Metals. *J. Am. Chem. Soc.* **2009,** *131* (40), 14381-14389.

(66) Ferrin, P.; Nilekar, A. U.; Greeley, J.; Mavrikakis, M.; Rossmeisl, J., Reactivity Descriptors for Direct Methanol Fuel Cell Anode Catalysts. *Surf. Sci.* **2008,** *602* (21), 3424-3431.

(67) Vandamme, N.; Janssens, E.; Vanhoutte, F.; Lievens, P.; Van Haesendonck, C., Scanning Probe Microscopy Investigation of Gold Clusters Deposited on Atomically Flat Substrates. *J. Phys.: Condens. Matter* **2003,** *15* (42), S2983-S2999.

(68) Fairley, N., *CasaXPS Manual 2.3. 15: Introduction to XPS and AES*. Casa Software, **2009**.

(69) Singh-Miller, N. E.; Marzari, N., Surface Energies, Work functions, and Surface Relaxations of Low-Index Metallic Surfaces from First Principles. *Phys. Rev. B* **2009,** *80* (23).

(70) Hutter, J.; Iannuzzi, M.; Schiffmann, F.; VandeVondele, J., CP2K: Atomistic Simulations of Condensed Matter Systems. *Wiley Interdiscip. Rev.: Comput. Mol. Sci.* **2014,** *4* (1), 15-25.

(71) VandeVondele, J.; Krack, M.; Mohamed, F.; Parrinello, M.; Chassaing, T.; Hutter, J., QUICKSTEP: Fast and Accurate Density Functional Calculations Using a Mixed Gaussian and Plane Waves Approach. *Comput. Phys. Commun.* **2005,** *167* (2), 103-128.

(72) Goedecker, S.; Teter, M.; Hutter, J., Separable Dual-Space Gaussian Pseudopotentials. *Phys. Rev. B* **1996,** *54* (3), 1703-1710.

(73) Hirshfeld, F. L., Bonded-Atom Fragments for Describing Molecular Charge-Densities. *Theor. Chim. Acta* **1977,** *44* (2), 129-138.

Insert Table of Contents artwork here